Available online at www.sciencedirect.com
SCIENCE DIRECT®
Earth and Planetary Science Letters 245 (2006) 509–522
EPSL
www.elsevier.com/locate/epsl

In situ sensing of methane emissions from natural marine hydrocarbon seeps: A potential remote sensing technology

Ira Leifer [a,*], Dar Roberts [b,1], Jack Margolis [c], Frank Kinnaman [d]

[a] Marine Sciences Institute, University of California, Santa Barbara, CA 93106, USA
[b] Geography Department, University of California, Santa Barbara, CA 93106, USA
[c] Remote Sensing Associates, Altadena, CA, USA
[d] Marine Sciences, University of California, Santa Barbara, CA 93106, USA

Received 30 September 2005; received in revised form 17 January 2006; accepted 20 January 2006
Available online 11 April 2006
Editor: M.L. Delaney

Abstract

The sources and sinks of methane, an important greenhouse gas, are poorly constrained. Remote sensing techniques can significantly improve our understanding of the global methane budget. Field and laboratory studies using in situ direct and spectral measurements of methane emissions from natural marine seepage allowed assessment of the feasibility of remote sensing. Methane plume characteristics were estimated by repeated transects of an intense marine seep area with a flame ion detector (FID) and then fit with a Gaussian plume to allow calculation of methane column abundances. These showed values greater than 0.5 g m^{-2} to a downwind distance of 70 m. A numerical radiative-transfer calculation showed that in the spectral region between 2200 and 2340 nm, which is sensitive to methane, there is mild sensitivity to water vapor interference, and that methane levels were well above the noise equivalent delta radiance of the Airborne Visible Infrared Imaging Spectrometer (AVIRIS). During a separate field study, FIDs recorded methane concentrations at 2.2, 3.6, and 5-m height while transecting an active seep area and concurrently collecting spectra using a field spectrometer. Several plumes were identified and a peak concentration of 200 ppm was measured. The presence of methane plumes along the incident path, as determined from the FID data, was related to the presence of methane absorption features in spectra above atmospheric background, which were absent outside the plumes.

Keywords: methane; remote sensing; spectral; in situ measurement; bubble plume; atmospheric plume; hydrocarbon seep; marine

1. Introduction

1.1. Overview

Understanding global climate change requires comprehensive budgets of greenhouse gases—atmospheric concentrations, sources, and sinks. Two of the most important greenhouse gases that are affected by human activities are carbon dioxide, CO_2, and methane, CH_4. Although the greenhouse warming per molecule of CH_4

* Corresponding author. Tel.: +1 805 893 4931.
E-mail addresses: ira.leifer@bubbleology.com (I. Leifer), dar@geog.ucsb.edu (D. Roberts), jacksm@earthlink.net (J. Margolis), frank_kinnaman@umail.ucsb.edu (F. Kinnaman).
[1] Tel.: +1 805 893 2276.

0012-821X/$ - see front matter © 2006 Elsevier B.V. All rights reserved.
doi:10.1016/j.epsl.2006.01.047

is at least 20 times stronger than CO_2 [1], its sources are poorly quantified. For example, total fossil fuel-related emissions of CH_4 are estimated at 120±40 Tg yr^{-1}, while agricultural sources may contribute from 115 to 345 Tg yr^{-1} [2]. Better understanding of the sources and sinks of CH_4 is important because its mixing ratio has more than doubled during the last century [3], increasing about 0.9% yr^{-1} until a recent acceleration [4].

The global atmospheric CH_4 budget is 540 Tg yr^{-1} with important natural sources such as wetlands and termites and anthropogenic sources including fossil-fuel derived CH_4, ruminants, and biomass burning [5]. Geologic sources are neglected in the budgets, although current global flux estimates suggest terrestrial and marine seepage contributes 35–45 Tg yr^{-1} [6], i.e., ~7% of the total budget. Thus, seep emissions are comparable to other important sources, such as termites [1]. The marine contribution for seeps was estimated conservatively at 20 Tg yr^{-1} [7] and arises primarily from methane hydrates and thermogenic sources.

Remote sensing improves atmospheric greenhouse gas measurements by allowing measurement at multiple scales with standardized measures and repeat sampling. Although no CH_4-specific, satellite-based remote-sensing platform currently is in orbit, several sensors can map CH_4 (Table 1). These sensors include the Scanning Imaging Absorption Spectrometer for Atmospheric Chartography (SCIAMACHY), the Infrared Atmospheric Sounding Interferometer (IASI), the Tropospheric Emission Spectrometer (TES), and the Atmospheric InfraRed Sounder (AIRS) [8–12]. CH_4 sensitive wavelengths on SCIAMACHY include 8 channels, of which channel #8 samples CH_4 absorption bands between 2265 and 2380 nm at a spectral resolution of 0.3 cm^{-1}. The IASI and TES include Fourier Transform InfraRed (FTIR) spectrometers designed for vertical atmospheric sounding of temperature and humidity. Spectral resolution in these sensors varies from several cm^{-1} for AIRS to 0.35 cm^{-1} for IASI to 0.1 cm^{-1} (apodized) on TES. AIRS is a dispersive, thermal IR spectrometer that generates temperature and humidity profiles with high precision and vertical resolution [12] with complete spectral coverage from 3.5 to ~15 μm, thus enabling CH_4 profiling by observation of the ν_4 band at 7.660 μm. However, the Ground Instantaneous Field of View (GIFOV) of these sensors is generally coarse, ranging from ~30 km along track and ~240 km across track at nadir for SCHIAMACHY [8] to the 9–12 km circular nadir GIFOV of IASI. Thus, while the spectral characteristics of these instruments are adequate for determining CH_4 column-abundances [10] or concentration profiles in the free atmosphere, spatial resolutions are inadequate for observations of heterogeneous small-scale sources (kilometer or smaller). Furthermore, there is a critical need for ground-reference data.

Table 1
Summary of methane-capable satellite platforms

Spectrometer	Spectral range (nm)	Spectral resolution (cm^{-1})	Nadir footprint (km×km)
SCIAMACHY	2265–2380	0.3	30×240
IASI	650–2760	0.35	9 to 12 circular
TES	15,400–5000	0.1	0.8×8
AIRS	15,000–3500	[1200*]	13.5×13.5

SCIAMACHY (Scanning Imaging Absorption Spectrometer for Atmospheric Chartography), IASI (Infrared Atmospheric Sounding Interferometer), TES (Tropospheric Emission Spectrometer), AIRS (Atmospheric InfraRed Sounder).
* The AIRS resolving power is $1200=\lambda/\Delta\lambda$.

We conducted field and laboratory studies using in situ measurements in an area of natural marine hydrocarbon seeps. Due to the relative spectral uniformity of the sea surface, the locality of the seeps, their clear identification by the visual and acoustic presence of bubbles, and the freedom of movement at sea, marine hydrocarbon seeps are an *ideal natural laboratory* to develop and ground-reference CH_4 remote sensing approaches. The study identified clearly distinct methane plumes with length scale order 10–100 m for use in validation studies. Radiative transfer calculations based on the field data tested the feasibility of using the Airborne Visible/Infrared Imaging Spectrometer (AVIRIS) platform. AVIRIS samples reflected radiance from 350 to 2500 nm at a nominal spectral sampling of 10 nm. Its IFOV is 1 mrad, producing a nominal GIFOV of 20 m and from 3 to 5 m, from the ER-2 and Twin Otter research airplanes, respectively (The ER-2 is the civilian equivalent of the stratospheric U-2 spy plane) [13]. Thus, AVIRIS can image small, local sources with sufficiently fine spectral sampling to detect numerous trace gases. AVIRIS represents the highest quality, publicly available, mobile imaging spectrometer for the solar spectrum. This study is a necessary first step towards ground-referencing methane remote sensing observations.

1.2. Hyperspectral atmospheric measurements

CH_4 is one of four major atmospheric gaseous absorbers with measurable absorptions in the visible–near infrared reflected solar spectrum. The dominant

absorber is H_2O vapor. The ability to retrieve column H_2O vapor using an imaging spectrometer such as AVIRIS is well established [13–18]. For example, Roberts et al. [17] documented the strong inverse relationship between column H_2O vapor and elevation, describing the seasonality of this relationship. Absolute humidity was estimated with a linear relationship between column H_2O vapor and elevation that matched ground measurements well.

AVIRIS can retrieve other trace gases. CO_2 also has three significant absorptions in this spectral region at 1970, 2010, and 2060 nm and several weaker absorptions centered near 1600 nm. This study took advantage of strong CH_4 absorptions between 2200 and 2400 nm and a second set of weaker absorptions near 1674 nm. Absorptions by CO_2 and CH_4 are quite evident (Fig. 1). Here, CO_2 and CH_4 absorption coefficients were calculated at a 1-nm spectral interval from spectral lines in the HITRAN-2004 database [19]. The calculation assumed a Lorentz Shape function for 1 atm at 296 K and used Loschmidt's number to convert from cm^2/molecule to cm^{-1} [20]. Stronger absorptions by CH_4 compared to CO_2 are evident centered near 2300 nm. Within the Earth's atmosphere, however, CO_2 absorptions are considerably stronger than CH_4 due to its much higher column-concentrations (370 ppm versus 1.9 ppm: Fig. 1—upper trace). For example, when simulated with MODTRAN 4v3.1 radiative transfer code [21] at a 10 cm^{-1} spectral resolution with a 5 cm^{-1} full-width half maximum (FWHM) from 25,000 to 4000 cm^{-1} prior to convolution, transmittance decreases to as low as 20% within the ~1950 nm CO_2 bands, but no lower than 80% around ~2350 nm for CH_4.

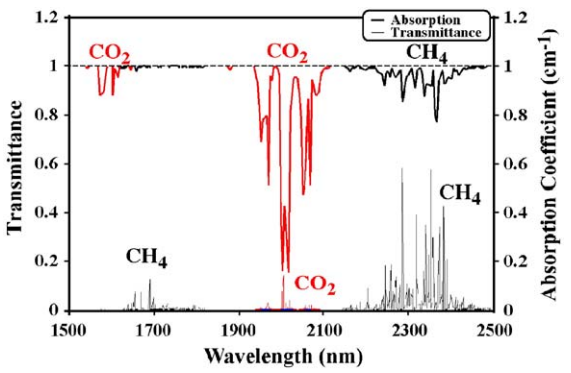

Fig. 1. Methane, CH_4 (black), and carbon dioxide, CO_2 (red), atmospheric transmission (upper) and absorption (lower) coefficients. Absorption calculated from HITRAN 2004 [19] at a 1 nm spectral interval, assuming a Lorentz Shape function at standard temperature and pressure and atmospheric transmittance calculated using MODTRAN 4v3.1. CH_4 and CO_2 bands are labeled on the figure. Transmission simulations assumed a mid-latitude airmass and temperate atmosphere and were convolved to a 5-nm full-width half-maximum and spectral sampling. (For interpretation of the references to colour in this figure legend, the reader is referred to the web version of this article.)

2. Methods

2.1. Study area

Studies were conducted in the Coal Oil Point (COP) seep field, in the Santa Barbara Channel, California, which has been studied extensively for decades and is one of the largest and best-known active marine seepage areas (Fig. 2). Studies have quantified seep area [22–24], emission flux using sonar techniques [25,26], ocean chemistry [27], and emissions with a direct gas capture device [28,29]. During the period 1995 to 2002, ~1.0–1.5×10^5 m^3 dy^{-1} seep gas entered the atmosphere while a roughly equal amount dissolved into the ocean [27].

The seeps are located above anticlines in hydrocarbon reservoirs along three trends. The inner trend is at 20-m depth and includes the informally named Shane and Brian seeps. There is a middle trend and a deeper trend at ~70 m that includes the Seep Tent seeps [30]. The Seep Tent seeps are near large seabed structures that capture gas emissions from an extremely intense seep area [31].

This study focused on CH_4 plumes from the Shane Seep area (34°24.370′N, 119°53.428′W, 22-m deep), and the Seep Tent seep area (34°23.063′N, 119°53.395′W, 70-m deep). During the study period, the Shane Seep area contained the most intense seepage and contributed significantly to total COP seep field emissions. Shane Seep has been investigated intensively for several years, including bubble [32] and fluid dynamics measurements [27,33], geochemical sampling [27], and flux measurements [28,29]. Flux measurements at Shane Seep by a direct-capture flux-buoy recorded some of the highest flux values per square meter for the entire COP seep field [29]. The surface expression of Shane Seep is characterized by several intense bubble plumes which create strong upwelling flows in the water column, and a much larger, dispersed plume from innumerable small vents at the seabed (order 10^3). The Seep Tent seep area produced the highest emissions in the seep field and was the most extensive, covering order 10^4 m^2, and had two highly prominent, intense bubble plumes.

2.2. In situ methane plume characterization approach

To establish conditions for CH_4 detection, seep emissions were measured. We used in situ measurements of total hydrocarbon (THC) with portable Flame Ion Detectors (FID), (OVA-88, Foxboro). The FIDs

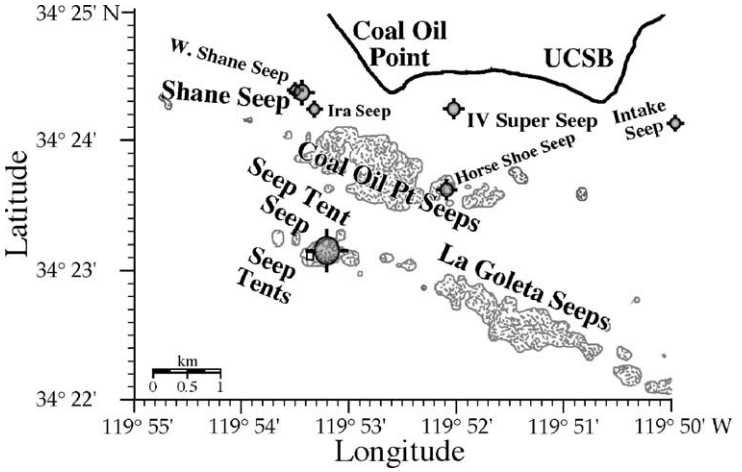

Fig. 2. Location of informally named seeps in the Coal Oil Point seep field, Santa Barbara Channel off the coast of Santa Barbara, California. Gray areas indicate regions of high bubble density from sonar returns [25]. Inshore seeps (Shane Seep, IV Super Seep, and Brian (Intake) Seep) were too shallow for the survey.

were calibrated prior to usage at the Southern California Gas Co., Engineering Analysis Center (SoCal-EAC) and are accurate to ~0.1 ppm, much less than background levels. A multi-channel data logger (OMP-MODL, Omega Corp, CT) acquired FID voltage outputs at 4 Hz. Data then were converted to THC mixing ratios using calibration curves. Air samples were collected ~15 cm above the center of the main bubble plume of Shane Seep in 1-L Teflon bags (SKC, PA) and were analyzed by SoCal-EAC. Wind speeds and directions were recorded with a hand-held anemometer (OMP-MODL, Omega, CT). Water and air temperatures were measured with mercury bulb thermometers.

Measurements were made from a small (7-m) Boston Whaler boats, whose low (~1 m) profile minimally affects wind streamlines. Differential GPS (NAD-83, Furama, Japan) was recorded every few seconds. Surveys recorded transects across the plumes, which allowed generation of a two-dimensional map of THC concentrations.

To estimate fluxes, measured concentrations were modeled as a Gaussian plume where the downwind surface concentration, C, is [34]:

$$C(x,y) = 2\pi\sigma_y(x)\sigma_z(x)Que^{-\frac{1}{2}\left(\frac{y}{\sigma_y(x)}\right)^2} e^{-\frac{1}{2}\left(\frac{z+h}{\sigma_z(x)}\right)^2} \quad (1)$$

where x, y, and z are the downwind, transverse, and vertical distances from the source, respectively, σ_y and σ_z are the horizontal and vertical diffusion coefficients, respectively, Q is the source strength, u is the wind speed, and h is the emission height, which is traditionally the smokestack height, or the height a buoyant plume rises before cooling to ambient and ceasing rising. For the seeps, h is assumed zero, because even though CH_4 is lighter than air, it is still a small fraction of the total plume gas. Both σ_y and σ_z are described by functions of x that depend upon atmospheric stability, which depends upon solar insolation, surface roughness, and u. For example, for slightly unstable conditions for light sun and winds ($3<u<4$ m s^{-1}) or for moderate sun and light winds ($2<u<3$ m s^{-1}) and surface roughness typical of the ocean at 3 m s^{-1}, Briggs turbulence yields [34]:

$$\sigma_y = 0.11x/\sqrt{1+10^{-4}x};\ \sigma_x = 0.08x\sqrt{1+2x10^{-4}x}. \quad (2)$$

Thus, for C measured at a known distance from the source, Q can be calculated from Eq. (1). There is some uncertainty in the validity of equations for σ_y and σ_z for coastal conditions since the parameterizations for σ_y and σ_z in Eq. (2) were from land studies.

2.3. Hyperspectral method and analysis approach

Radiative transfer modeling used the MODTRAN 4. v3.1 radiative transfer code [21] to model reflected radiance as would be measured by AVIRIS. Our objective was to simulate radiance reflected off a specular surface beneath a CH_4 plume with varying column CH_4. Because variable H_2O vapor potentially can obscure a CH_4 signal, simulations were conducted for fixed CH_4 and variable column H_2O vapor. Column CH_4 was varied between background (1.0) and 1.05, 1.09, and 1.18 times background, corresponding to 0,

0.5, 1, and 2 g/m^2 of column CH_4 within a plume from Shane Seep. H_2O vapor was varied from dry to relatively moist conditions, equivalent to 0.64, 2.0, and 2.9 cm of precipitable water. Simulations were parameterized to match an AVIRIS ER-2 overflight over the Shane Seep area on 14 June 2001. Scene specific parameters included latitude (34°26.700′N), longitude (119°55.000W), time (20.2438 UTC), 30-km visibility, and mid-latitude summer model. The sea-surface reflectance was modeled as 100% relative to a Lambertian surface. Changes in sea-surface roughness alter the albedo, and in particular, sun glint, but not the spectral shape. Depending upon geometry, reflectance can be much greater or less than 100%. Thus, the sea surface state affects the threshold for detectability.

To aid interpretation of field spectra, laboratory spectra were measured for CH_4 with varying partial pressures and for seep gas collected at the seabed from Brian Seep (34°24.109′N, 119°49.917′W, 10-m deep). The lab and field studies used the same Analytical Spectral Devices (ASD) Full Range Instrument (ASD Inc., Boulder Colorado), thereby reproducing the instrument-specific characteristics of the field spectra, such as wavelength calibration, spectral response functions, artifacts, and signal-to-noise. The ASD is a grating instrument that samples between ~350 and ~2500 nm at a spectral sampling interval of 1.4 nm in the visible–near infrared (VNIR), 400–1000 nm, with a FWHM of 3–4 nm and an interval of 2.2 nm in the short wave infrared (SWIR), 1000–2500 nm, with a FWHM of 10–12 nm. Output spectra were re-sampled to a 1-nm interval. For the lab study, the ASD was operated in reflectance mode with a 50 spectrum spectral average and an 8° foreoptic. Sample transmittance was determined as a measure of light transmitted through a gas filled 10-cm path length quartz optical-cell after reflection off a spectralon panel (Labsphere, CO) normalized by light measured using the same light source, panel, and optical cell without a gas sample (Fig. 3). Illumination was by a 250-W quartz halogen bulb at a 45° angle. To minimize light contamination, the quartz optical cell was wrapped in foil and placed flush against the 8° foreoptic used with the ASD. Prior to each sample, the system was evacuated using a vacuum pump, followed by a reference standard measurement. Pressure was controlled and monitored with a 199.9–0 kPa pressure gauge (Model DPG1000B, Omega, CT) within the cell and standardized to 1 atm for each sample. CH_4 partial pressures were chosen to range from 185 mb (equivalent to 5% above atmospheric background from the height of the ER-2 flight on 14 June 2001) to 38 mb (20% of the upper partial pressure). CH_4 abundance was varied by changing the mixing ratio of each gas sample to nitrogen in the cell. Between samples, the cell was repeatedly pumped out and flushed with fresh air until there was no longer a spectral signature of the test gas. Then, the cell was refilled with the mixture of nitrogen and test gas. Four CH_4 (37.9, 72.4, 154, and 185 mb) and three seep gas mixtures (76.4, 147.4, and 777.9 mb) were measured and replicated when feasible.

The field intercomparison study was conducted 8 Oct. 2004. The ASD spectrometer was configured to collect

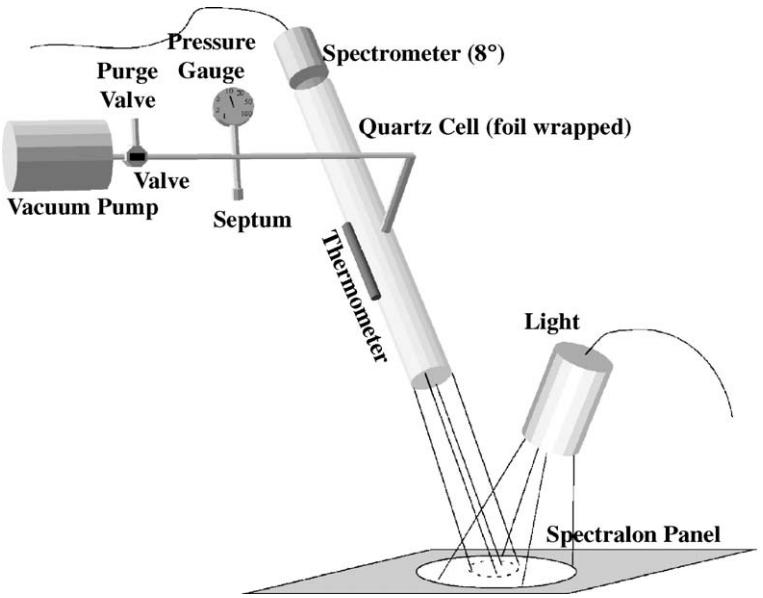

Fig. 3. Laboratory spectral experimental set-up.

50 spectra at 5-s intervals along each transect. Each spectrum was the average of 10 spectral measurements. The instrument was in reflectance mode, whereby a reference spectrum is collected for the spectralon panel and then divided into each subsequent spectrum measured from the same panel along the transect. This effectively allows cancellation of background absorptions. The instrument was configured with an 8° foreoptic which was positioned ~0.5 m from the panel. Ideally, normalizing spectra collected within the plume with a reference spectrum collected outside the plume will produce absorption features.

3. Results

3.1. Laboratory measurements of methane and seep gas

Laboratory transmittance of CH_4 gas showed the ASD can quantify CH_4 absorptions for the partial pressures studied (Fig. 4A). While the four fundamental CH_4 bands (ν_1 and ν_3 symmetric and asymmetric stretches and ν_2 and ν_4 bends) occur at longer wavelengths, overtones and combinations of the CH_4 Octad (2079–2967 nm) and Tetradecad (1618–2083 nm) are quite evident [35]. Furthermore, transmittance spectra showed an expected decrease in transmittance with an increase in CH_4 partial pressure, fitting a Beer–Lambert model for transmittance with $R^2 > 0.99$ for strong bands. Obvious H_2O vapor contamination is evident, with very strong H_2O vapor bands producing absorptions at 1830, 1870, and 1910 nm (Fig. 4A). These results suggest that CH_4 detection is feasible. For example, given a relatively poor signal to noise ratio of 200 : 1 (0.5%), a 4% decrease in transmittance at 37.9 mb implies that CH_4 anomalies 1/8th as large (4–5 mb) should be detectable near 2350 nm.

Transmittance spectra for seep gas from Brian Seep (Fig. 4C) are consistent with a CH_4 dominated gas. Gas chromatography (MicroGC, Agilent Technologies) showed that the gas was 91.2% CH_4, 7.5% CO_2, 1.1%

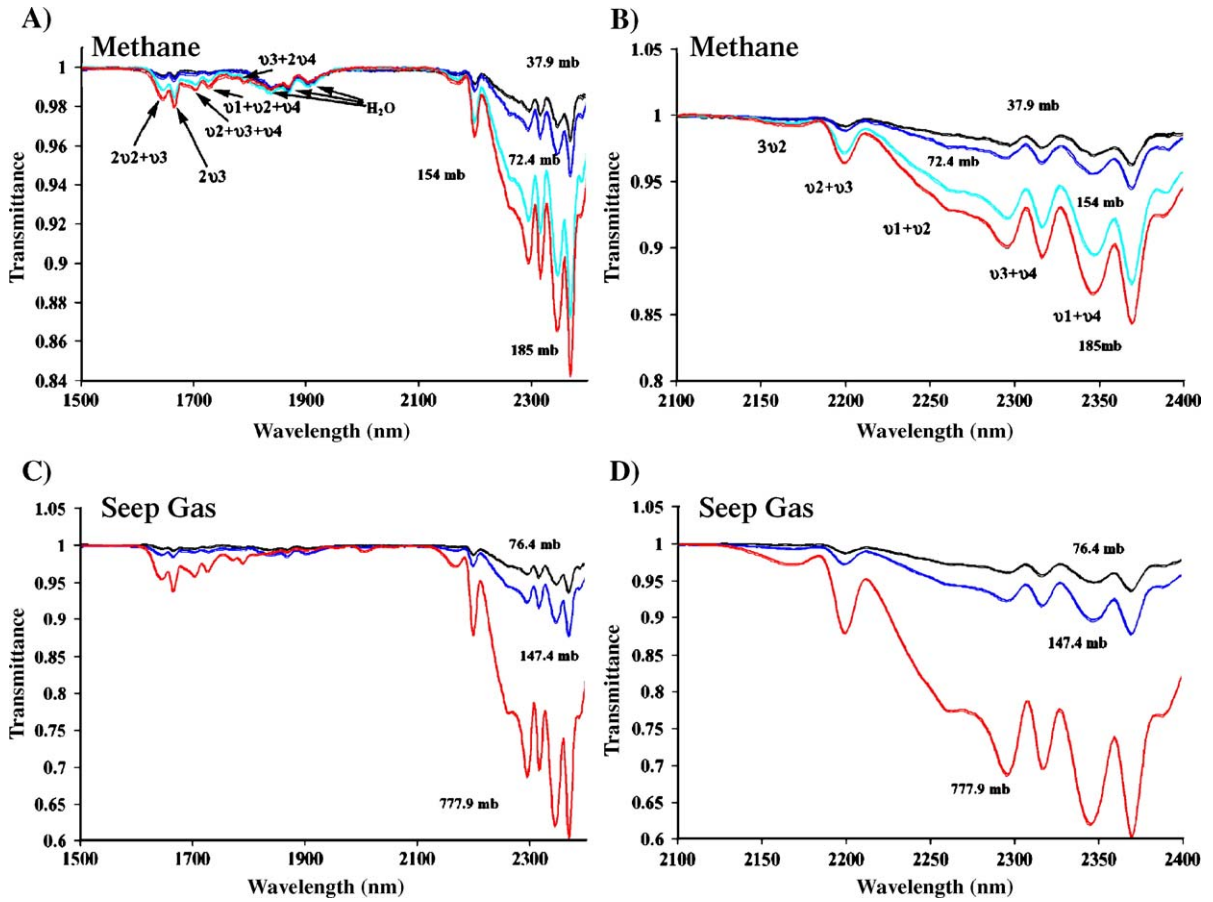

Fig. 4. (A) Laboratory methane transmittance for a range of methane partial pressures through a 10-cm optical cell. Remainder of cell is nitrogen. (B) Detail of spectrum from 2100 to 2400 nm. (C) Seep gas transmittance for a range of seep gas partial pressures. Remainder of cell is nitrogen. (D) Detail of spectrum from 2100 to 2400 nm. There was some water vapor contamination in all samples. Partial pressures noted on figure.

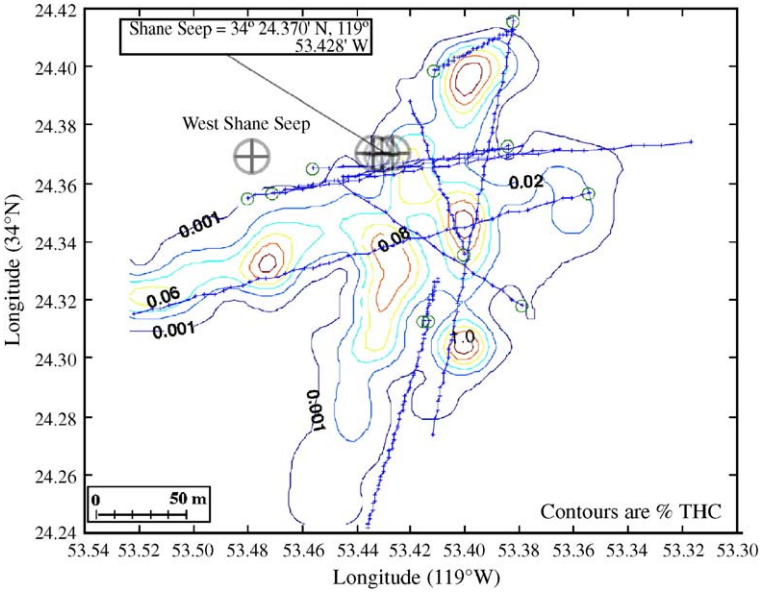

Fig. 5. Contour map of Shane Seep atmospheric total hydrocarbon (THC) concentration (%), 21 Nov. 2002. Lines show boat tracks, with ticks indicating measurement points and circles show transect starting points. The sea surface locations of major plumes of Shane Seep and W. Shane Seep are indicated by targets. Distance scale on figure. Measurements were gridded to 0.01′ latitude–longitude bins and measurements in each bin averaged. Winds were light (2 to 2.8 m s^{-1}) from WNW. Near surface currents were onshore, towards the north at ~0.5 m s^{-1}. The shoreline is NNE from Shane Seep.

C_2H_6, 0.2% C_3H_8, with trace n-C_4H_{10}, isomers, and higher *n*-alkanes. Other absorptions that were evident included minor H_2O vapor contamination between 1800 and 2000 nm and a modest absorption feature at 2014 nm, centered in the strongest CO_2 band in the SWIR. The latter feature was only evident at the highest seep gas partial pressure (778 mb).

3.2. Atmospheric methane FID plume measurements

Seabed gas from Shane Seep is 83% CH_4, 12% CO_2, 2% air gases, 3% ethane, with higher *n*-alkanes [33]. At the sea surface, the more soluble components have been stripped out, while air gases have exsolved. Atmospheric gas composition immediately above Shane Seep was 1.91% CH_4 with combined *n*-alkanes less than 0.02%—i.e., total hydrocarbons (THC) measured by the FIDs was almost entirely CH_4.

Atmospheric CH_4 plumes from distinct bubble plumes rapidly mix into a large plume that is advected downwind and diffuses laterally and vertically. To create a spatial plume map, the Shane Seep plume was transected repeatedly on 21 Nov. 2002. The resultant data was contoured and showed a plume with peak

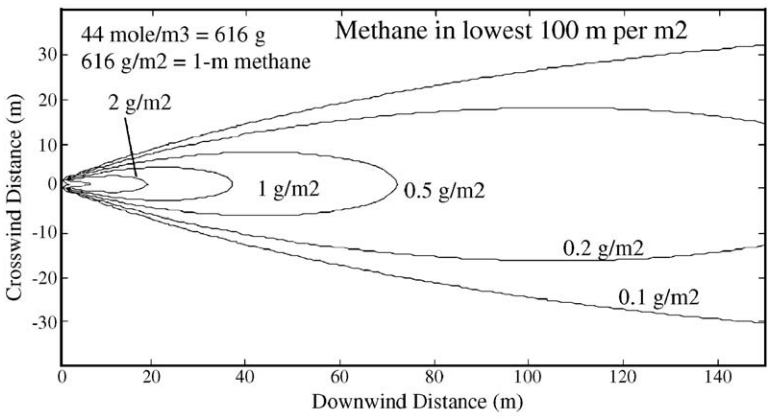

Fig. 6. Contour plot of vertical integration of Gaussian plume fit to observations shown in Fig. 5.

mixing ratios greater than 0.08% slightly downwind of Shane Seep (Fig. 5). West Shane Seep is an area of dispersed bubbles ~30 m west of the Shane Seep, which produced an atmospheric plume at 34°24.33′N, 119°53.47′W. The survey identified strong CH_4 sources from the main bubble plumes and also at 34°24.40′N, 119°53.40′W-NNE of Shane Seep. Because there were no bubbles in this region, it most likely (particularly given the currents) resulted from the sea to air flux from a dissolved CH_4 plume. The wind-driven plume trails offshore towards the south.

The contour plot shows CH_4 parallel to the sea surface and thus is orthogonal to the remote-sensing view line along the solar angle. A three-dimensional Gaussian plume was fit to the surface data and integrated to estimate the CH_4 column-height (Fig. 6). The calculation assumed Briggs turbulence for moderate sun, moderately stable conditions, and the measured 2.9 m s^{-1} wind speed. For this plume, over 99% of the CH_4 lay in the bottom 100 m within the first few hundred meters downwind from the source.

3.3. Spectral calculations for an AVIRIS sensor

To assess the feasibility of field spectral measurements with an AVIRIS type spectrometer, MODTRAN numerical simulations were performed based on field data (Fig. 6). Initial simulations demonstrate that although weak, CH_4 should be detectable by AVIRIS (Fig. 7). Although CO_2 and H_2O vapor dominate the spectrum, CH_4 produces detectable features between 2200 and 2400 nm. Analysis of residuals, subtracting background radiance from plume simulations, demonstrates that the highest and second highest column CH_4 simulations exceeded AVIRIS's Noise Equivalent Delta Radiance (NEDL) of 0.002 μm W cm^{-2} sr^{-1} (Fig. 7B and C). The lowest column CH_4 simulation of 0.5 g m^{-2} exceeded the NEDL by a factor of five. Furthermore, simulated radiance with CH_4 set at 1.18 times background–equivalent to 2 g m^{-2}–and variable column H_2O vapor demonstrates that although most of the spectral region between 2200 and 2340 nm is sensitive to CH_4, it is only mildly sensitive to changes in H_2O vapor.

3.4. Field intercomparison between FID and spectral data

On 8 Oct. 2004, three FIDs were mounted at 2.2, 3.6, and 5 m height to map CH_4 plumes. An example of these CH_4 measurements at the Seep Tent Seep including the boat location with time is shown in Fig. 8. Winds were very light from the SW and variable, with a

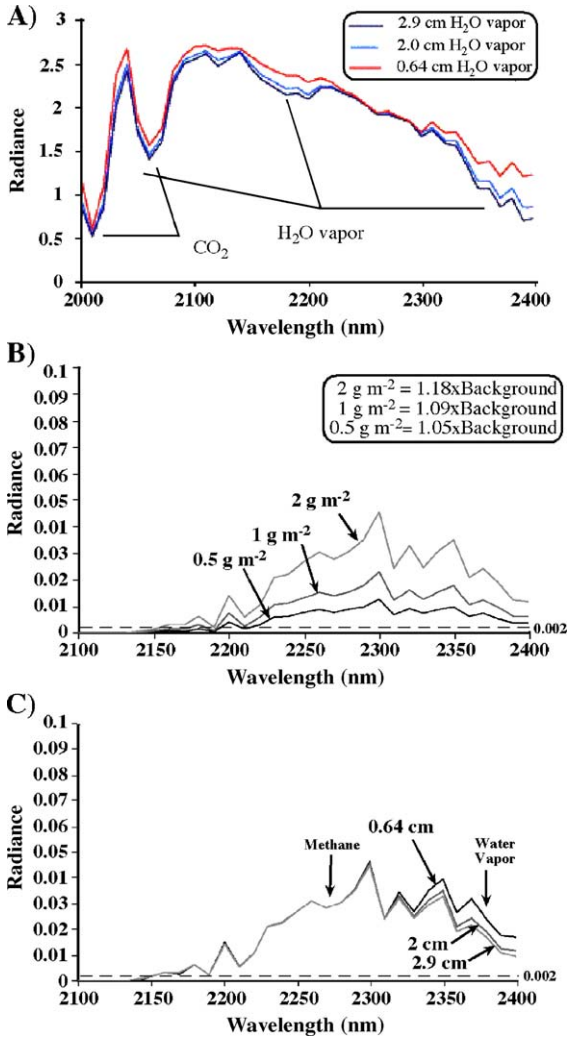

Fig. 7. (A) MODTRAN simulation of reflected radiance from a 100% reflectant surface with background CH_4 and variable column H_2O vapor of 0.64, 2.0, and 2.9 cm. (B) Radiance residuals from MODTRAN simulation after subtracting background radiance for various plume CH_4 columns and a 2-cm column H_2O vapor. (C) Radiance residuals for methane at 1.18 times background (2 g m^{-2}) and variable-column H_2O vapor. CH_4 and H_2O column heights labeled on figure. Dashed line at 0.002 radiance is noise equivalent delta radiance for AVIRIS.

solar zenith of 42.3° and solar azimuth of 205°. Due to the time of year, the solar angle was low, thus the vertical mounted FIDs and the path of the incidence radiation diverged significantly. Data were filtered with a 1-s low-pass filter to eliminate short (<0.25 s) transient electronic noise and the FID zero levels were improperly calibrated. These problems did not interfere with identification of atmospheric CH_4 plumes.

Two major atmospheric plumes are indicated, one with a source near the northeast jog at 13:50 LT (local time) when the boat was over a large bubble plume

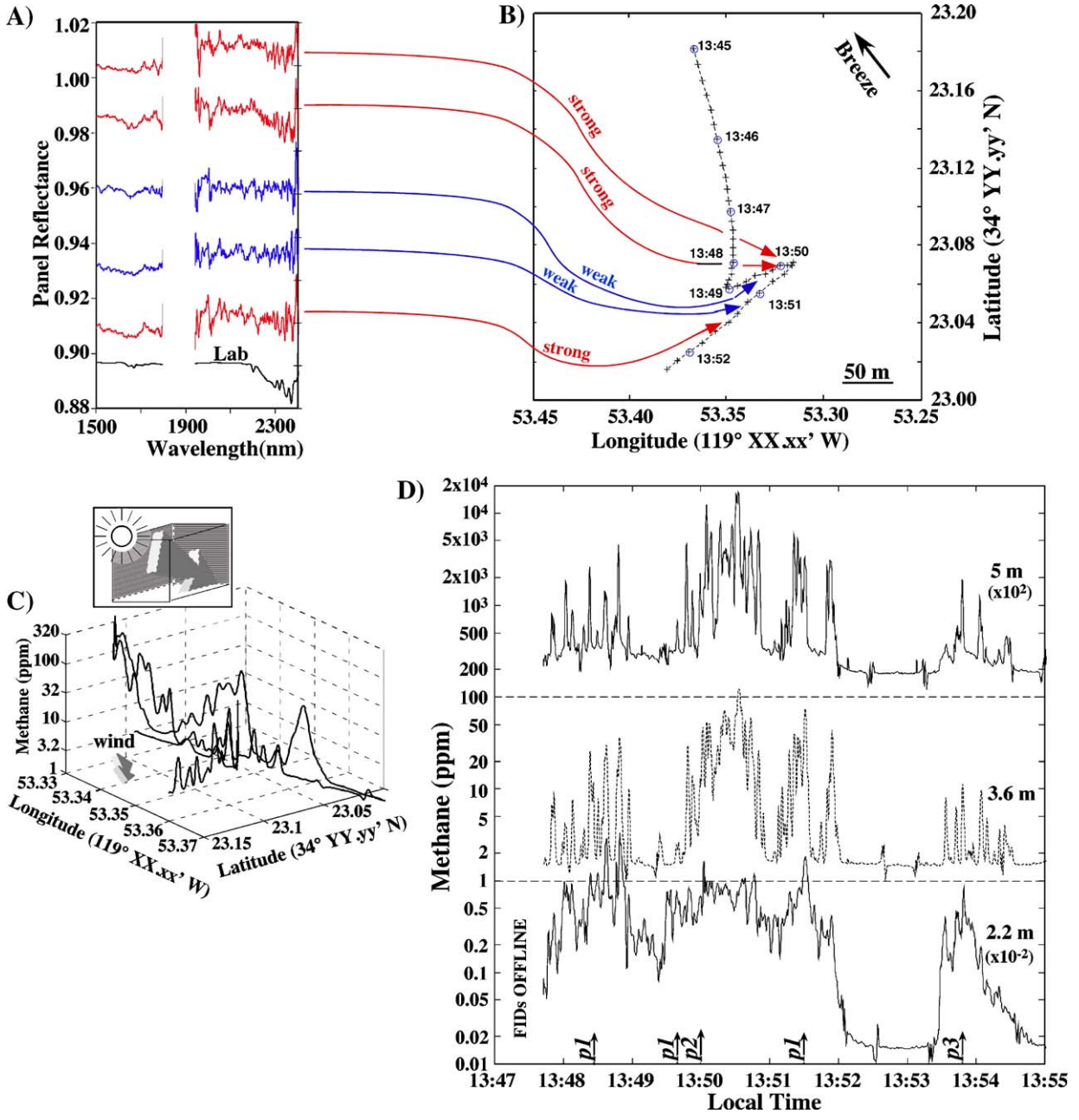

Fig. 8. (A) Spectra and (D) methane mixing ratios at three heights during a transect 8 October 2004 through the Seep Tent Seep area. Locations shown in (B), ticks are every 10 s, circles every minute with times noted on figure. Methane height labeled, 5-m height is multiplied by 100, 2.2-m height is multiplied by 0.01. Methane concentrations were smoothed with a 1-s low-pass filter. (C) Three-dimensional plot of transect methane data at 3.6-m height. Solar angle and wind direction on inset.

(p2) and a second plume (p1) originating to the south–southeast of the boat's position at 13:51 LT. This second plume was transected at 13:48:30, 13:49:50, and 13:51:30 LT. The last transect was closest to the source and had the highest concentrations at all three heights. There also were numerous smaller atmospheric plumes, such as one transected during the initial approach from the North (Fig. 8C). This is consistent with the vast spatial extent and heterogeneity of bubble plumes of the Seep Tent seep area. The most significant plume was at 13:50 LT, when the boat was in the center of the bubble plume. A distinct third plume was observed at 13:53:50 LT clearly at 2.2 m and weaker at the higher heights (p3).

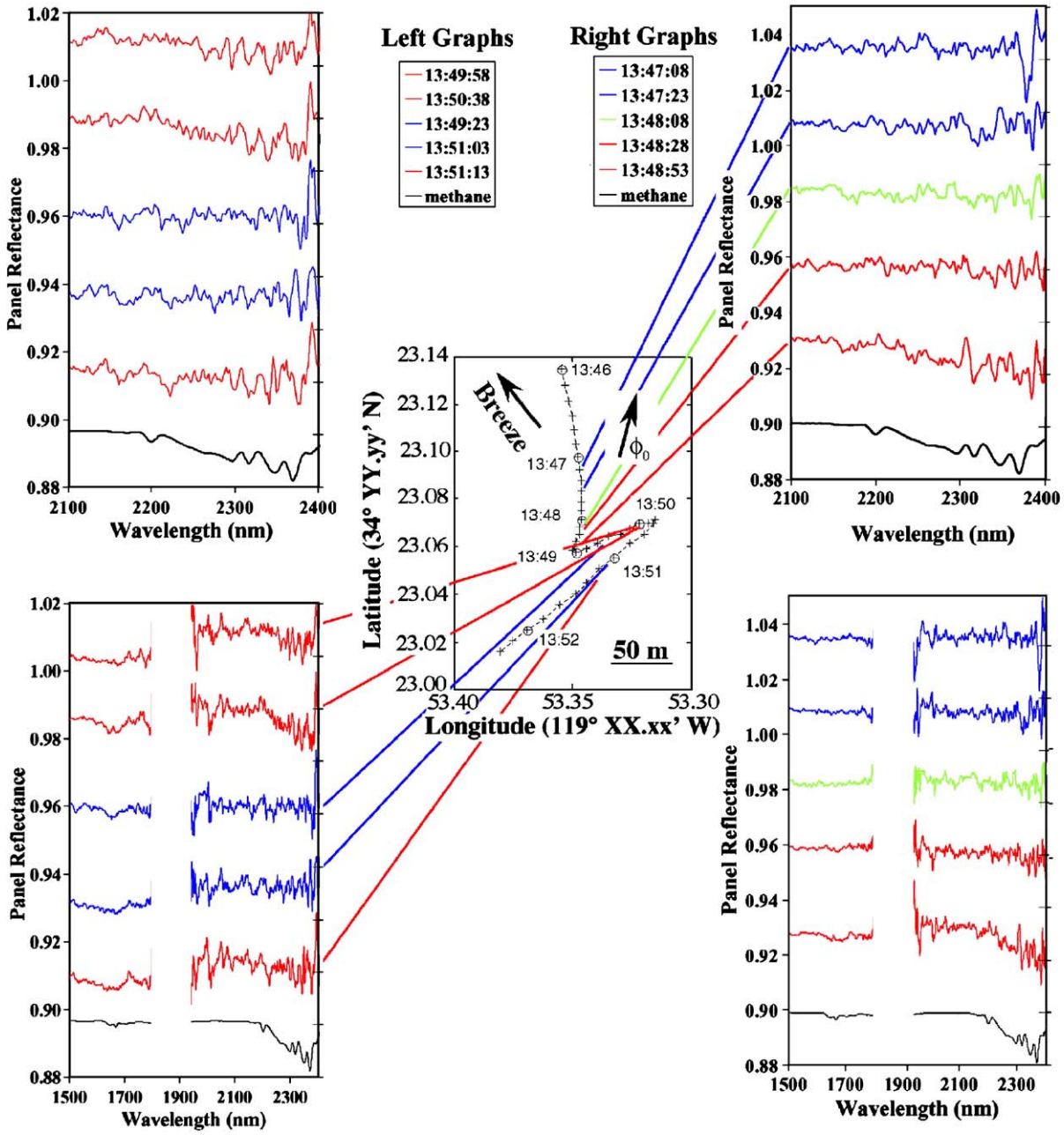

Fig. 9. Field spectra at various times along the boat trajectory showing strong methane absorption features (red), weak methane absorption features (blue), and intermediate absorption features (green). Upper panels show 2100 to 2400 nm wavelengths, while lower panels for a wider wavelength range (1500 to 2450 nm). In each panel, the lowest spectrum is from laboratory methane. Central panel shows boat trajectory. ϕ_o indicates solar direction (180° from the azimuth). Data key shows times (local time) of each spectrum.

The plumes exhibited considerable variability, which arises from temporal and spatial variability in emissions and atmospheric turbulence. The highest CH_4 value was almost 200 ppm at 5 m. Plumes were much more laterally extensive at lower heights. Above the main bubble plume (13:50:30 LT), there was little variation with height. In contrast, the concentration and spatial extent of the plume encountered at 13:48 LT decreased rapidly with height.

Spectra from this transect are shown in Fig. 9. Red spectra exhibited clear CH_4 signatures, while blue spectra did not exhibit clear CH_4 features, and green

spectra were intermediate. The best CH_4 features were for 13:50:38 LT–the center of the bubble plume–where the highest CH_4 concentrations were observed and where the CH_4 concentrations decreased little with height. The other strong spectra occurred in the vicinity of the second plume (p1), but slightly to the south. This was consistent with the solar angle, which was towards the south (−15° azimuth, from 180°).

In a non-buoyant Gaussian plume, the vertical extension of the CH_4 plume increases with downwind direction, while the vertical gradient decreases. In the main plume, the highest values were observed at the highest height, while there was a much greater vertical gradient, downwind (13:47:30 to 13:48:00 LT). These results, plus the weakness of the wind are all consistent with the plume rising buoyantly. Furthermore, a rising plume would explain the strong CH_4 spectral signature at 13:51:13 LT, upwind of the main bubble plume. A rising plume would have risen into the solar path.

4. Discussion

4.1. Method intercomparison

Both in situ FID and spectral approaches identified atmospheric CH_4 plumes from the seeps. Each method has advantages and disadvantages. The FID measurements are point observations with very high temporal (i.e., spatial) resolution and can observe fractional increases above background concentrations. However, to calculate the source strength—i.e., flux, requires estimation of a three-dimensional plume from what is at the best, several one-dimensional transects a few meters above the sea surface. Measuring CH_4 concentrations at several heights is an improvement, but data are still close to the sea surface. Although larger boats could expand the range of heights, they affect the wind streamlines much more.

The spectral approach observes total CH_4 absorption along the solar path. Because the sunlight passes through significant background atmospheric CH_4 (1.5 cm atm) before entering the plume, it is much less sensitive than the FID approach. This is particularly true for the ASD spectrometer, which lacks sufficiently fine spectral resolution to resolve individual CH_4 lines. A significant advantage of the spectral approach is that each transect observes a two-dimensional plane of the plume (at the solar angle). This eliminates the vertical estimation required by the FID approach to estimate source strength. However, this integration along the solar path decreases sensitivity to small-scale variability.

4.2. The Gaussian plume model

To derive the source strength based on a Gaussian plume for both approaches requires several conditions. The atmospheric plume must be well-mixed, thus observations cannot be too close to the source. Too far downwind the concentrations and path columns will decrease below detection limits. Light winds (<2–3 m/s) are often highly variable leading to difficulty in plume characterization. However, high winds significantly decrease plume concentrations and increase the difficulty of working at sea. Because CH_4 is lighter than air, high mixing-ratio plumes rise buoyantly until mixing decreases concentrations sufficiently. Buoyantly rising plumes, though, are difficult to interpret—i.e., what portion of the plume was transected. Buoyant plumes are likely at low wind speeds. Also, fitting data with a Gaussian plume requires repeated plume transects (e.g., Fig. 5) implying that conditions (emissions and meteorology) remain approximately constant during the transects. On 8 Oct. 2004 winds were very light, highly variable, and the plume likely was buoyant, thus, source strength estimation from this data set was not feasible.

Critical to source strength estimation are the wind speed, direction, variability (σ_y and σ_z) and turbulence characterization, which were estimated from on-board measurements. However, for airplane or satellite remote sensing, these parameters must be derived from other remote sensing observations. Aerial surveys resolve several of these problems by creating a two-dimensional map of the plume-column thickness integrated over each pixel's spatial area. Also, by looking down vertically, they are unaffected by buoyant rise. Variability at low wind speed still is a problem and can lead to low column abundances in many pixels. In contrast, high wind speed decreases plume concentrations and widths, potentially to less than a pixel dimension, decreasing the CH_4 column abundance averaged over the pixel.

4.3. Methane spectral measurements

Lab spectra demonstrate that the ASD can quantify CH_4 absorptions, even at the lowest partial pressures tested and showed that the seep gas was primarily CH_4 with detectable CO_2 and were consistent with independent analysis of seep–gas composition. Field spectra from the CH_4 plumes were consistent with the laboratory results. In situ field CH_4 concentrations were as high as 200 ppm at 2-m and 100 ppm at 5-m height. When integrated over a 5-m thick column, a 100 ppm concentration translates to column abundance

of ~0.05 cm atm roughly 1/8th the lowest partial pressure measured in the laboratory. Furthermore, it is not surprising that the best correlations between field spectra and FIDs were observed for CH_4 detected at the 5-m level, which translates to the longest pathlength through the CH_4 plume. Significant CH_4 absorptions were not observed when CH_4 was not detected by the FIDs, which occurred when the solar path and CH_4 plumes did not intersect or when CH_4 was only found at the lowest height; closest to the plume source. Also, several spectra collected near the strongest CH_4 sources showed prominent CH_4 features at 1650 nm.

Field spectra were collected under suboptimal environmental conditions such as lower solar angles than during the summer and atmospheric haze. Although haze has minimal impact on the SWIR, it nevertheless modifies total incoming solar radiation and may provide some increased radiative scattering. Improvements in signal to noise can be achieved by increasing the pathlength between the foreoptic and reflective panel. Also, the use of a reference measurement outside the plume is based on the assumption of a relatively invariant background atmosphere along a transect. However, as demonstrated by radiative transfer models and lab spectra, even a minor change in background H_2O vapor along a transect potentially could generate H_2O vapor artifacts. We suspect that the primary reason that CH_4 bands at 2200 and 2370 nm, which were observed in the laboratory spectra but were not observed in the field was due to obscuration by strong H_2O vapor bands in these spectral regions.

4.4. Numerical calculations

Based upon radiative transfer simulations for the field data and AVIRIS's noise equivalent delta radiance, CH_4 plumes should be highly detectable at resolutions for the Twin Otter (3 to 4 m resolution) and ER-2 (20-m resolution) airplanes. For the plume in Fig. 6, the Twin Otter should be able to observe CH_4 column abundances of 2, 1, 0.5, and 0.2 g m^{-2}, representing 5, 27, 94, and 419 pixels and 0.12, 0.6, 2.1, and 9.4 pixels for the ER-2, respectively. Thus, AVIRIS from the Twin Otter should resolve the source area as a region of highest localized concentration and the downwind, expanding plume. Given wind speed and plume geometry, it should be possible to estimate the CH_4 flux. From the ER-2, AVIRIS would not resolve the highest concentration sources, but would detect the presence of a plume and its direction of propagation. Also, while AVIRIS's spectral resolution cannot resolve individual spectral lines, it can resolve overtones and combinations, especially in the region centered around 2300 nm (with little H_2O-vapor confusion). While the mid-IR (3–5 μm) is widely recognized as superior due to the presence of stronger CH_4 fundamental absorptions in Earth's atmosphere, the stronger spectral lines can become saturated. Furthermore, this spectral region involves a mixture of terrestrial emitted and solar-reflected radiance, which complicates the spectral analysis.

The radiative transfer simulations identify spectral regions with minimal confusion between CH_4 and H_2O. Because H_2O vapor and CH_4 tend to vary independently, improvement of CH_4 detection should be possible by first solving for H_2O column abundance and then solving for CH_4 with constrained H_2O vapor. In this manner, CH_4 could be solved using multiple CH_4 bands, minimizing errors by minimizing residuals between predicted and measured radiance for both CH_4 and H_2O vapor.

4.5. Applicability of remote sensing to other marine and terrestrial sources

Similar remote sensing approaches and techniques as used at marine seeps could be applied to marshlands at high tide. However, for terrestrial CH_4 sources, variability in the surface composition and hence spectral response introduce additional complexities. For example, higher spatial heterogeneity on land would result in changes in reflected radiance independent of the CH_4 plume and may contribute spectral structure to reflected radiance that overlaps with CH_4 bands. However, the spectral width of CH_4 features is several orders of magnitude narrower than the width of most terrestrial features. Also, lower surface reflectance will effectively reduce the signal to noise ratio.

A follow-on, remote sensing study of methane plumes is planned to determine an optimum design for an aircraft borne instrument. Critical needs are determination of the accuracy of plume column amounts for such a device based on retrieval algorithms to be developed. The study also will determine how remote sensing of methane plumes can improve understanding of methane sources and sinks and climate.

5. Conclusion

The feasibility of using a remote sensing approach to measure atmospheric CH_4 emissions was tested through laboratory and field studies and radiative transfer simulations for a marine natural hydrocarbon seep source. Field studies used simultaneous in situ and spectral CH_4 measurements during transects of seepage

areas. These data represent the first attempt to use atmospheric measurements to investigate marine seep emissions. There was very good correlation between the in situ CH_4 plume observations and the appearance of CH_4 absorption features in spectra where the solar pathlength passed through the CH_4 plumes. CH_4 absorption features were confirmed by spectra obtained from the laboratory studies. Furthermore, the in situ approach identified atmospheric CH_4 sources from both bubble transport and air–water exchange from a dissolved plume.

Using a Gaussian plume model of in situ CH_4 plume measurements for a seep area, radiative transfer calculations strongly support that CH_4 signatures from the seeps are within AVIRIS capabilities for a range of typical conditions. Using AVIRIS to identify CH_4 emissions from the seeps should be feasible from both Twin Otter and ER-2 airplanes. AVIRIS accuracy would be improved if both water vapor and CH_4 were retrieved simultaneously.

Acknowledgements

We would like to thank the support of the U.S. Mineral Management Service, Agency #1435-01-00-CA-31063, Task #18211, the University of California Energy Institute, and NSF #OCE-0447395. Special thanks to Leigh Brewer, Sempre Utilities, for in situ methane measurements and Marc Moritsch, Santa Barbara County Air Pollution Control District, for providing data from West Campus air pollution Station. Views and conclusions in this document are those of the authors and should not be interpreted as necessarily representing the official policies, either expressed or implied of the U.S. government, or UCSB. Thanks also to Jet Propulsion Laboratory for the use of the ASD spectrometer.

References

[1] M.A.K. Khalil, R.A. Rasmussen, The changing composition of the Earth's atmosphere, in: H.B. Singh (Ed.), Composition, Chemistry, and Climate of the Atmosphere, Van Nostrand Reinhold, New York, 1995, pp. 50–97.

[2] J. Lelieveld, P.J. Crutzen, F.J. Dentener, Changing concentration, lifetime and climate forcing of atmospheric methane, Tellus 50B (1998) 128–150.

[3] F.S. Rowland, Methane and chlorocarbons in the earth's atmosphere, Orig. Life 15 (1985) 279.

[4] K.A. Kvenvolden, Potential effects of gas hydrate on human welfare, Proc. Nat. Acad. Sci. 96 (1999) 3420–3426.

[5] M. Prather, R. Derwent, D. Erhalt, P. Fraser, E. Sanhueza, X. Zhou, Other trace gases and atmospheric chemistry, in: J.T. Houghton, L.G. Meira Filho, J. Bruce, H. Lee, B.A. Callander, E. Haites, N. Harris, K. Maskell (Eds.), Climate Change 1994, Radiative Forcing of Climate Change and an Evaluation of the IPCC IS92 Emission Scenarios, Cambridge University Press, Cambridge, United Kingdom, 1995, pp. 77–119.

[6] G. Etiope, R.W. Klusman, Geologic emissions of methane into the atmosphere, Chemosphere 49 (2002) 779–791.

[7] K.A. Kvenvolden, W.S. Reeburgh, T.D. Lorenson, Naturally occurring methane seepage—Workshop report, EOS 82 (2001) 457.

[8] H. Bovensmann, J.P. Burrows, M. Buchwitz, J. Frerick, S. Noel, V.V. Rozanov, K.V. Chance, A.P.H. Goede, SCIAMACHY: mission objectives and measurement modes, J. Atmos. Sci. 56 (1999) 127–150.

[9] F. Aires, A. Chedin, N.A. Scott, W.B. Rossow, A regularized neural net approach for retrieval of atmospheric and surface temperatures with the IASI instrument, J. Appl. Met. 41 (2002) 144–159.

[10] F. Artuso, P. Chamard, A. di Sarra, S. Piacentino, F. Thiery, Measurement of atmospheric methane in the Mediterranean, Proceedings 8th International Global Atmospheric Chemistry Conference, Christchurch, New Zealand, 2004.

[11] R. Beer, T.A. Glavich, D.M. Rider, Tropospheric emission spectrometer for the earth observing system's aura satellite, Appl. Optics 40 (2001) 2356–2367.

[12] T.S. Pagano, H.H. Aumann, D. Hagan, K. Overoye, Prelaunch and in-flight radiometric calibration of the atmospheric infrared sounder (AIRS), IEEE Trans. Geosci. Remote Sens. 41 (2003) 343–351.

[13] R.O. Green, M.L. Eastwood, C.M. Sarture, T.G. Chrien, M. Aronsson, B.J. Chippendale, J.A. Faust, B.E. Pavri, C.J. Chovit, M.S. Solis, M.R. Olah, O. Williams, Imaging spectroscopy and the airborne visible infrared imaging spectrometer, Remote Sens. Environ. 65 (1998) 227–248.

[14] C.J. Bruegge, J.E. Conel, J.S. Margolis, R.O. Green, G. Toon, V. Carrere, R.G. Holm, G. Hoover, In-situ atmospheric water-vapor retrieval in support of AVIRIS validation, in: G. Vane (Ed.), Imaging Spectroscopy of the Terrestrial Environment, Proceedings of the SPIE Meeting, Orlando, Fl, April 16–17, 1990, The International Society for Optical Engineering (SPIE), Bellingham, WA, 1990, pp. 150–163.

[15] R.O. Green, J.E. Conel, D.A. Roberts, Estimation of aerosol optical depth, pressure elevation, water vapor and calculation of apparent surface reflectance from radiance measured by the airborne visible–infrared imaging spectrometer (AVIRIS) using MODTRAN2, in: G. Vane (Ed.), SPIE Conf. 1937, Imaging Spectrometry of the Terrestrial Environment, The Society of Photo-Optical Instrumentation Engineers, Orlando, FL, 1993, pp. 2–5.

[16] B.C. Gao, K.B. Heidebrecht, A.F.H. Goetz, Derivation of scaled surface reflectances from AVIRIS data, Remote Sens. Environ. 44 (1993) 165–178.

[17] D.A. Roberts, R.O. Green, J.B. Adams, Temporal and spatial patterns in vegetation and atmospheric properties from AVIRIS, Remote Sens. Environ. 62 (1997) 223–240.

[18] S. Ogunjemiyo, D.A. Roberts, K. Keightley, S.L. Ustin, T. Hinkley, B. Lamb, Evaluating the relationship between AVIRIS water vapor and poplar plantation evapotranspiration, J. Geophys. Res. Atmos. 107 (2002) 20-1–20-15.

[19] L.S. Rothman, D. Jacquemart, A. Barbe, D. Chris Benner, M. Birk, L.R. Brown, M.R. Carleer, C. Chackerian Jr., K. Chance, L. H. Coudert, V. Dana, V.M. Devi, J, -M. Flaud, R.R. Gamache, A.

Goldman, J.M. Hartmann, K.W. Jucks, A.G. Maki, J.-Y. Mandin, S.T. Massie, J. Orphal, A. Perrin, C.P. Rinsland, M.A.H. Smith, J. Tennyson, R.N. Tolchenov, R.A. Toth, J. Vander Auwera, P. Varanasi, G. Wagner. The HITRAN 2004 molecular spectroscopic database. J. Quant. Spectroscopy Radiative Trans (in press).

[20] J.T. Houghton, The Physics of Atmospheres, 2nd edition. Cambridge University Press, Cambridge, 1986, 271 pp.

[21] A. Berk, G.P. Anderson, L.S. Bernstein, P.K. Acharya, H. Dothe, M.W. Matthew, S.M. Adler-Golden, J.H. Chetwynd Jr., S.C. Richtsmeier, B. Pukall, C.L. Allred, L.S. Jeong, M.K. Hoke, MODTRAN4 radiative transfer modeling for atmospheric correction, Proceedings of SPIE Optical Spectroscopic Techniques and Instrumentation for Atmospheric and Space Research III, 19–21 July, 1999, pp. 1–6.

[22] A.A. Allen, R.S. Schlueter, P.G. Mikolaj, Natural oil seepage at Coal Oil Point, Santa Barbara, California, Science 170 (1970) 974–977.

[23] P.J. Fischer, A.J. Stevenson, in: P.J. Fischer (Ed.), Natural Hydrocarbon Seeps, Santa Barbara Basin, California, in Santa Barbara Channel Area Revisited Field Trip Guidebook, vol. 3, Am. Assoc. Petrol Geol., Tulsa, Okla, 1973, pp. 17–28.

[24] D.C. Quigley, Spatial and temporal quantification of gaseous natural marine hydrocarbon seeps in the Santa Barbara Channel, California. Master Thesis, University of California, Santa Barbara, 1997, p. 95.

[25] J.S. Hornafius, D. Quigley, B.P. Luyendyk, The world's most spectacular marine hydrocarbon seeps (Coal Oil Point, Santa Barbara Channel California): quantification of emissions, J. Geophys. Rev. 104 (1999) 20703–20711.

[26] D.C. Quigley, J.S. Hornafius, B.P. Luyendyk, R.D. Francis, J. Clark, L. Washburn, Decrease in natural marine hydrocarbon seepage near Coal Oil Point, California, associated with offshore oil production, Geology 27 (1999) 1047–1050.

[27] J.F. Clark, L. Washburn, J.S. Hornafius, B.P. Luyendyk, Natural marine hydrocarbon seep source of dissolved methane to California coastal waters, J. Geophys. Res. 105 (2003) 11509–11522.

[28] L. Washburn, C. Johnson, C. Gotschalk, E.T. Egland, A gas-capture buoy for measuring bubbling gas flux in oceans and lakes, J. Atmos. Ocean. Technol. 18 (2001) 1411–1420.

[29] L. Washburn, J.F. Clark, P. Kyriakidis, The spatial scales, distribution, and intensity of natural marine hydrocarbon seeps near Coal Oil Point, California, Mar. Pet. Geol. 22 (2005) 569–578.

[30] I. Leifer, J. Boles, J.F. Clark, B.P. Luyendyk, The dynamic nature of marine hydrocarbon seepage, Environ. Geol. 46 (2004) 1038–1052.

[31] W. Rintoul, ARCO caps Santa Barbara Channel seep, Pac. Oil World 74 (1982) 6–9.

[32] I. Leifer, J. Boles, Measurement of marine hydrocarbon seep flow through fractured rock and unconsolidated sediment, Mar. Pet. Geol. 22 (2005) 551–568.

[33] I. Leifer, J.F. Clark, R.F. Chen, Modifications of the local environment by a natural marine hydrocarbon seep, Geophys. Res. Lett. 27 (2000) 3711–3714.

[34] S.R. Hanna, G.A. Briggs, R.P. Hosker Jr., in: J. Smith (Ed.), Handbook on Atmospheric Diffusion, Technical Information Center, U.S. Department of Energy, 1982, p. 101.

[35] L.R. Brown, D.C. Benner, J.P. Champion, V.M. Devi, L. Fejard, R.R. Gamache, T. Gabard, J.C. Hilico, B. Lavorel, M. Loete, G. Ch. Mellau, A. Nikitin, A.S. Pine, A. Predoi-Cross, C.P. Rinsland, O. Robert, R.L. Sams, M.A.H. Smith, S.A. Tashkun, V.G. Tyuterev, Methane line parameters in HITRAN, J. Quant. Spectrosc. Radiat. Transfer 82 (2003) 219–238.